

General Torque Enhancement Approach for a Nine-Phase Surface PMSM with Built-in Fault Tolerance

Original

General Torque Enhancement Approach for a Nine-Phase Surface PMSM with Built-in Fault Tolerance / Slunjski, Marko; Stiscia, Ornella; Jones, Martin; Levi, Emil. - In: IEEE TRANSACTIONS ON INDUSTRIAL ELECTRONICS. - ISSN 0278-0046. - ELETTRONICO. - 68:8(2021), pp. 6412-6423. [10.1109/TIE.2020.3007053]

Availability:

This version is available at: 11583/2846074 since: 2021-02-15T11:06:23Z

Publisher:

IEEE

Published

DOI:10.1109/TIE.2020.3007053

Terms of use:

This article is made available under terms and conditions as specified in the corresponding bibliographic description in the repository

Publisher copyright

IEEE postprint/Author's Accepted Manuscript

©2021 IEEE. Personal use of this material is permitted. Permission from IEEE must be obtained for all other uses, in any current or future media, including reprinting/republishing this material for advertising or promotional purposes, creating new collecting works, for resale or lists, or reuse of any copyrighted component of this work in other works.

(Article begins on next page)

General Torque Enhancement Approach for a Nine-Phase Surface PMSM with Built-in Fault Tolerance

Marko Slunjski, *Student Member, IEEE*, Ornella Stiscia, *Student Member, IEEE*, Martin Jones, Emil Levi, *Fellow, IEEE*

Abstract—The paper investigates maximum possible torque improvement in a two-pole surface permanent magnet synchronous machine (PMSM) with a reduced magnet span, which causes production of highly non-sinusoidal back-EMF. It contains a high third and fifth harmonics, which can be used for the torque enhancement, using stator current harmonic injection. Optimal magnet span is studied first and it is shown that with such a value the machine would be able to develop an insignificantly lower maximum torque than with the full magnet span. Next, field-oriented control (FOC) algorithm, which considers all non-fundamental EMF components lower than the machine phase number, is devised. Using maximum-torque per Ampere (MTPA) principles, optimal ratios between fundamental and all other injected components are calculated and then used in the drive control. The output torque can be in this way increased up to 45% with respect to the one obtainable with fundamental current only. Alternatively, for the same load torque, stator current RMS value can be reduced by 45%. Last but not least, a method for position sensor fault mitigation is introduced. It is based on the alternative use of a back-EMF harmonic for rotor position estimation, instead of the torque enhancement. Experimental verification is provided throughout for all the relevant aspects.

Index Terms—Multiphase drives, PMSM, non-sinusoidal back-EMF, harmonic current injection, position sensor fault.

I. INTRODUCTION

Multiphase PMSMs are a growing area of research interest due to the dual benefits offered by the multiphase stator winding and permanent magnet rotors. They have found utility in high-power, high reliability applications, such as automotive [1], traction [2], marine [3] and aerospace [4] industries. Enhanced torque density is in these applications highly desirable and, over the past 30 years, multiphase machines have been investigated extensively as means to achieve this goal [5]. They possess additional degrees of freedom that can be used to inject current harmonics into the stator windings. In an n -phase machine, all odd low-order harmonic components between 1 and n can be used to couple with the corresponding spatial MMF harmonics to yield additional torque contributions.

Five-phase machines have been studied the most [3]–[16]. In [6] a 20-slot concentrated winding five-phase PMSM with almost trapezoidal EMF is proposed. It is shown that, by injection of the third harmonic current, the machine has better performance than its three-phase and five-phase BLDC counterparts, while offering greater controllability. The work in [7] takes a three-phase 2.1 MW PMSM podded propeller motor

and reconfigures it into a five-phase fractional slot machine, with full pole pitched radial magnets in order to boost the third harmonic torque component. The new machine provides 15% higher torque and 71% lower torque pulsations with the same copper losses. A 20-slot 8-pole five-phase concentrated winding machine with winding factors of 0.588 for the fundamental and 0.951 for the third harmonic is studied in [1]. A dual-harmonic interior magnet rotor is designed, using 16 additional magnets, to improve the third harmonic flux and boost the torque by 33% in the base speed region. The third harmonic also boosts the torque in a five-phase surface PMSM in [8]. By shaping the magnets to produce third harmonic flux and injecting third harmonic current 1/6 of the fundamental, the torque is increased by 30% while maintaining low torque ripple.

In [9] a fractional-slot concentrated winding five-phase machine with a dual-harmonic rotor is developed by making holes in the middle of the rotor pole pitch. An interior magnet dual-harmonic rotor with holes, similar to [9], is designed in [10] to produce a five-phase concentrated winding machine whose torque is produced equally by the first and the third harmonic of current and EMF. During operation in the base speed region the classical maximum torque-per-ampere MTPA control method is employed while in the field weakening region a maximum torque per losses (MTPL) method is used. A five-phase 20-slot 8-pole dual-harmonic machine with surface magnets is developed in [3] in order to reduce torque ripple. FE analysis is used to select a suitable rotor leading to a two-thirds pole arc design. The resulting machine is capable of reducing the torque ripple by more than three times when compared to the equivalent three-phase machine. Magnet shaping with third-harmonic flux within the same flux limit is another rotor topology developed in [11], [12]. Related to this approach, the unequal stator tooth width, PM segmentation and Halbach array [13]–[15] are among the latest five-phase machine topologies aimed at boosting the torque using harmonic current injection.

Optimal level of the third harmonic current injection has been investigated in [10], [16]–[18]. In [10], the MTPA method, combined with the stator current RMS constraint, was used. A computationally efficient vectorial approach to determine the optimal current references to minimize stator copper losses in a five-phase PMSM with trapezoidal back EMF during normal and faulted operation is introduced in [17].

Multiphase PMSMs with $n > 5$, which utilize higher harmonic current components, have been investigated to a far lesser extent. A six-phase PMSM was studied in [18], [19], where the 5th and the 7th harmonic injection was considered. It is shown that the torque can be increased by 8.6% with negligible torque ripple. Seven-phase dual-harmonic PMSMs are modelled and control systems developed for healthy and

faulted operation in [20], [21]. A further interesting research, related to the low-order harmonic utilisation in n -phase machines, was presented in [22], where a novel heuristic algorithm for symmetrical fractional slot concentrated winding multiphase PMSM design, which maximizes the output average torque under the current harmonic injection, was developed. A nine-phase interior PMSM is investigated in [23] utilising the 3rd, 5th and 7th harmonic injections. Using the method of third harmonic current injection, developed in [10] for a five-phase PMSM, it was shown in [24] that the use of the third harmonic current in a nine-phase PMSM of a very specific construction, discussed shortly, enables $\approx 36\%$ higher output torque while enabling a significant reduction of the permanent magnet material use in the machine. A nine-phase consequent pole machine is proposed in [25]. The machine is composed of semi-inset type magnets (12 magnet poles) and laminated iron poles (12 iron poles) with a segmented rotor and the aim is to reduce the amount of PM material for use in EV applications.

This paper builds on [24], [26] and [27]. A nine-phase PMSM, designed with a significantly reduced amount of PMs, is analysed first, from the point of view of the relationship between PM span and the achievable torque production. In contrast to, say [3], where a fractional slot PMSM was considered, the machine is with an integer slot number per phase per pole. The design does not require reshaping of magnets or specialized rotor structures. It is shown that almost the same torque can be achieved with the optimal magnet span of app. 70° as in the machine with 180° span. Next, the field oriented control scheme is extended to take into account all meaningful back-EMF harmonics produced by the shortened magnet span. Back-EMF based MTPA method is employed for optimal ratio calculation for different current harmonics. Finally, a back-EMF harmonic based rotor position estimation is introduced, for the first time, as a means for fault-tolerant operation in the case of the encoder/resolver failure. The complete control scheme, including fault-tolerant control, is validated using an experimental platform.

The paper is organised as follows. Machine topology is described in Section II, where the optimal magnet span is analysed as well. Section III introduces the FOC algorithm for torque improvement, while Section IV discusses optimal harmonic injection ratios. Principles of position sensorless control for fault tolerant purposes are described in Section V. Experimental validation is given in Section VI, followed by the conclusions of the paper in Section VII.

II. INVESTIGATED NINE-PHASE PMSM

A. Basic Machine Data

The cross section of the studied machine is shown in Fig. 1, [24]. The machine was obtained by rewinding a three-phase six-pole MOOG FAS T-2-M2-030 machine (180 V, 8.5 A, 1.73 kW, 3000 rpm, 150 Hz) and removing four NdFeB magnets from the rotor. Known data and electrical parameters of the nine-phase configuration are given in Table I, while flux and experimentally recorded back-EMF (Fig. 2a) harmonics (Fig. 2b) are characterised with the values shown in Table II. The stator of the machine has 36 slots.

If compared with the existing methods for torque improvement, the used magnet shaping (i.e. reduction of the amount of magnet material, by reducing the magnet span to 45° , to produce high harmonic content in the back-EMF spectrum) is different. New rotor structure gives rise to a highly non-

sinusoidal back-EMF (Fig. 2a), in which, in addition to the high third harmonic (92.7% of the fundamental), a significant fifth (49.8%) and small seventh (12.8%) harmonics also exist (Fig. 2b). These odd harmonics can be used to boost torque. Hence, the new rotor structure was analysed first in detail using a finite element (FE) software (similar as in [24]), and compared to the alternatives, as reported in the next sub-section.

B. Impact of Magnet Span on Total Torque Production

As the first step, the machine described in the previous sub-section is compared to an equivalent two-pole machine with 180° magnet span. All the other data of the machine remain the same. In such a machine the back-EMF and its spectrum at 1500 rpm (25 Hz) would be as shown in Fig. 3. In addition to the fundamental, a small third harmonic exists. Although this EMF component can also be used for torque boost, this is initially not taken into account. By applying the phase current RMS value in motoring mode as equal to $1/\sqrt{2}$ A, average electromagnetic torque is obtained as app. 2.92 Nm (Fig. 4). This increases to 2.99 Nm (i.e. ≈ 3 Nm) if the third harmonic boost is used.

Since the machine used here has two magnets with 45° span, the same FE analysis is repeated for the actual machine, using again phase current RMS value as $1/\sqrt{2}$ A. The study is done for the use of fundamental only, and the combined 1st, 3rd and 5th harmonic. Torque waveforms are shown in Figs. 5a and 5b, respectively. Average torque values are app. 1.68 and 2.39 Nm.

The magnet span used here (45°) is not optimal. Using the same approach as in [24], a study is performed to find the optimal magnet span under the condition of the 1st, 3rd and 5th harmonic injection. The rounded value comes out as 70° , yielding the average torque of 2.9 Nm.

Fig. 6 illustrates achievable average torque under the condition of the same RMS current for different magnet spans and different injection scenarios. It can be seen that, with respect to the maximum achievable value of 3 Nm with 180° span, use of 70° sacrifices around 3% of the average torque, while span of 45° yields a reduction of 20%. These values look favourable, considering the reduction in the use of PM material, which is for the 45° magnet span one quarter of that required for the 180° span.

As is obvious from the given considerations, the study conducted here assumed that the magnet thickness is invariant, resulting in a change of magnet volume and mass as the magnet

TABLE I. MACHINE DATA AND PARAMETERS.

Quantity/value	$f_n = 50$ Hz	$L_{d1} = L_{q1} = L_1 = 459.8$ mH
$V_n = 220$ V	$R_s = 31.3$ Ω	$L_{d3} = L_{q3} = L_3 = 120.4$ mH
$n_n = 3000$ rpm	$L_b = 84.7$ mH	$L_{d5} = L_{q5} = L_5 = 96.0$ mH

TABLE II. BACK-EMF AND FLUX LINKAGE HARMONICS (PEAK VALUES) OF THE PMSM.

Order	back-EMF [V]	$n = 1463.5$ rpm (24.39 Hz)	PM flux [mWb]
1	$e_1 = 59.13$		$\lambda_{m1} = 385.83$
3	$e_3 = 54.81$		$\lambda_{m3} = 119.22$
5	$e_5 = 29.37$		$\lambda_{m5} = 38.34$
7	$e_7 = 7.54$		$\lambda_{m7} = 7.03$

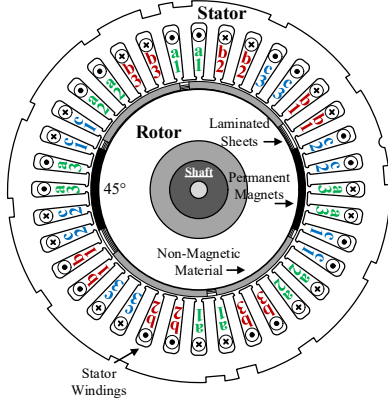


Fig. 1. Cross-section of the nine-phase surface mounted PMSM prototype.

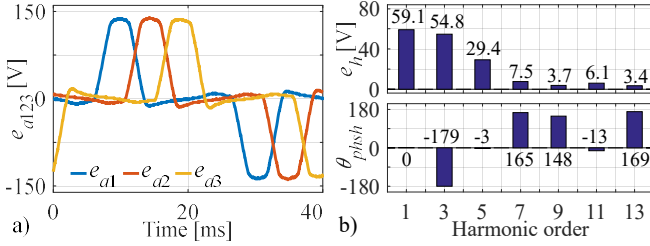


Fig. 2. Experimentally recorded back-EMF (a) and its harmonic spectrum (b).

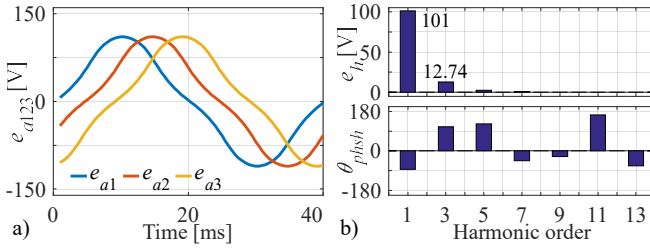


Fig. 3. Back-EMF (a) and its harmonic spectrum (b) in an equivalent 180° magnet span machine.

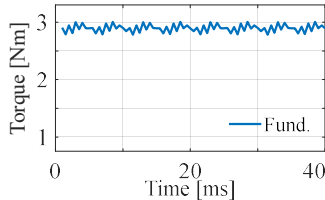


Fig. 4. Torque obtained at 25 Hz by FE for 180° magnet span using fundamental only ($T_{em} \approx 2.92$ Nm).

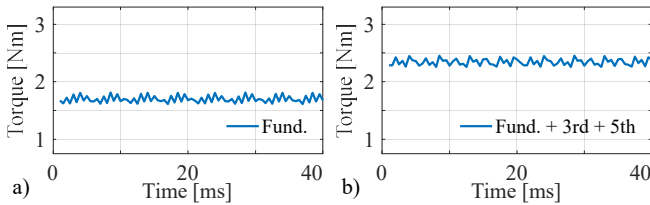


Fig. 5. Electromagnetic torque at 25 Hz for 45° magnet span: for fundamental current only (a) ($T_{em} \approx 1.68$ Nm) and with the 1st, 3rd and 5th harmonic currents (b) ($T_{em} \approx 2.39$ Nm).

span changes. An alternative way of doing the comparison would be to keep the magnet volume invariant, while varying both the magnet span and the magnet thickness.

In the study reported in this section the RMS current is, as noted, kept the same. Subdivision of the current into the first and other harmonics (where appropriate) is done using the method and values reported in Section IV.

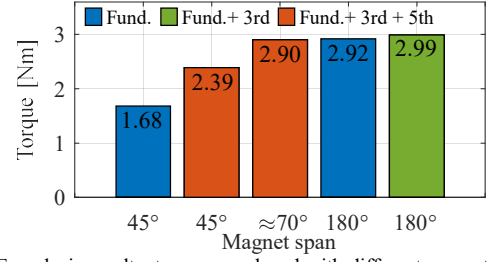


Fig. 6. FE analysis results: torques produced with different magnet spans and different harmonic current injection (the same phase current RMS of $1/\sqrt{2}$ A).

III. GENERAL FIELD-ORIENTED CONTROL APPROACH FOR SURFACE PMSM HARMONIC CURRENT INJECTION

Surface PMSM modelling for the case of stator current harmonic injection is in principle well-known, e.g. [6], [17], [26]. Denoting with h the harmonic order, equivalent d - q circuits for the h^{th} harmonic can be represented as shown in Fig. 7, using multiple synchronous reference frames representation. Hence model equations can be formulated by knowing only the h^{th} harmonic order values of permanent magnet flux (λ_{mh}), stator winding self-inductance (L_{dh} , L_{qh}), and the angular speed ω_{el} :

$$v_{dh} = R_s i_{dh} + \frac{d\psi_{dh}}{dt} - h\omega_{el}\psi_{qh}; \quad v_{qh} = R_s i_{qh} + \frac{d\psi_{qh}}{dt} + h\omega_{el}\psi_{dh} \quad (1)$$

$$\psi_{dh} = L_{dh} \cdot i_{dh} + \lambda_{mh}; \quad \psi_{qh} = L_{qh} \cdot i_{qh} \quad (2)$$

$$T_{emh} = \frac{n}{2} \cdot P \cdot h \cdot \lambda_{mh} \cdot i_{qh} \quad T_{em} = \sum_{h=1,3,5,\dots} T_{emh} \quad (3)$$

Assuming PI current control in multiple synchronous reference frames, stator and decoupling voltages for the h^{th} order harmonic on the outputs of current PI regulators are:

$$v_{dh-reg} = R_s i_{dh} + L_{sh} \frac{di_{dh}}{dt}; \quad v_{qh-reg} = R_s i_{qh} + L_{sh} \frac{di_{qh}}{dt} \quad (4)$$

$$e_{dh} = -h\omega_{el}(L_{sh} \cdot i_{qh}); \quad e_{qh} = h\omega_{el}(L_{sh} \cdot i_{dh} + \lambda_{mh}) \quad (5)$$

Rotational transformation can be for the h^{th} order component transformation modified by adding the rotational transformation for corresponding pair of rows as:

$$\begin{bmatrix} \dots \\ i_{dh} \\ i_{qh} \\ \dots \end{bmatrix} = \begin{bmatrix} \dots & \dots & \dots & \dots \\ \dots & \cos(h\theta + \theta_{phsh}) & \sin(h\theta + \theta_{phsh}) & \dots \\ \dots & -\sin(h\theta + \theta_{phsh}) & \cos(h\theta + \theta_{phsh}) & \dots \\ \dots & \dots & \dots & \dots \end{bmatrix} \begin{bmatrix} \dots \\ i_{xj} \\ i_{yj} \\ \dots \end{bmatrix} \quad (6)$$

In (6), θ_{phsh} stands for the h^{th} harmonic angular shift, subscript j represents auxiliary subspace in which the corresponding harmonic is mapped, and x - y stand for components in auxiliary subspaces obtained after VSD transformation.

Ratios of fundamental torque-producing current i_{q1} and torque-producing currents of the harmonic components i_{q3} , i_{q5} , ..., i_{qh} can be represented with k_{13} , ..., k_{1h} as:

$$k_{13} = \frac{i_{q3}}{i_{q1}}; \quad k_{15} = \frac{i_{q5}}{i_{q1}}; \quad \dots, \quad k_{1h} = \frac{i_{qh}}{i_{q1}} \quad (7)$$

The number of torque-producing components in the total electromagnetic torque governs the number of required current injection harmonic controllers. Relation between fundamental torque-producing current i_{q1} , total electromagnetic torque T_{em} and defined ratios k_{13} , k_{15} , ..., k_{1h} suitable for FOC implementation can be described in the general case as:

$$i_{q1} = \frac{2}{n \cdot P} \cdot \frac{T_{em}}{\lambda_{m1} + 3 \cdot \lambda_{m3} \cdot k_{13} + 5 \cdot \lambda_{m5} \cdot k_{15} + \dots + h \cdot \lambda_{mh} \cdot k_{1h}} \quad (8)$$

A schematic of the FOC algorithm for any number of desired harmonic current injections is shown in Fig. 8. Since the control scheme is applied here in conjunction with a nine-phase machine, PI current controllers are used in the first d - q plane for the fundamental current, as well as in the other two planes in which the third and the fifth current harmonic map. There are therefore two pairs of current controllers of the form shown in the blue rectangle of Fig. 8. When any of these two harmonics is not used for torque enhancement, the currents in that plane are forced to zero using the PI controllers.

It is important to note that, if a low-order harmonic is not utilized for torque enhancement (or any other purpose), then the stator current for that harmonic needs to be eliminated. This is the situation encountered in the x - y plane in which the seventh current harmonic would flow. As the PM flux for the seventh harmonic is minute, torque is not enhanced with this harmonic and the plane is not used for a different purpose either. Hence the currents in this plane are forced to zero using vector proportional integral (VPI) resonant controllers [28], operated in the stationary reference frame. This current control is performed as shown in Fig. 8 (bottom part, on the right-hand side of the coordinate transformation block), in the “VPI resonant current controllers” block.

IV. THE OPTIMAL HARMONIC CURRENT INJECTION RATIOS

A study examining how adding stator current harmonics affects the torque production and stator current RMS values is conducted next. A simple torque/injection ratio (T_{em}/k) analysis is used and the torque function is solved for all ratios from [0-2] interval. From the corresponding plot, maximum torque value is determined. Disregarding the seventh harmonic, relationship between torque T_{em} and two current injection ratios k_{13} , k_{15} is:

$$T_{em} = \frac{n \cdot P}{2} \cdot (\lambda_{m1} i_{q1} + 3\lambda_{m3} i_{q3} + 5\lambda_{m5} i_{q5}) \quad (9)$$

$$k_{13} = \frac{i_{q3}}{i_{q1}}; k_{15} = \frac{i_{q5}}{i_{q1}} \rightarrow T_{em} = \frac{n \cdot P}{2} \cdot (\lambda_{m1} + 3\lambda_{m3} k_{13} + 5\lambda_{m5} k_{15}) \cdot i_{q1}$$

$$T_{em} = \frac{n \cdot P}{2} \cdot (\lambda_{m1} i_{q1} + 3\lambda_{m3} i_{q3} + 5\lambda_{m5} i_{q5}) \quad (10)$$

$$k_{13} = \frac{i_{q3}}{i_{q1}}; k_{15} = \frac{i_{q5}}{i_{q1}} \rightarrow T_{em} = \frac{n \cdot P}{2} \cdot (\lambda_{m1} + 3\lambda_{m3} k_{13} + 5\lambda_{m5} k_{15}) \cdot i_{q1}$$

$$T_{em} = \frac{nP}{2} \cdot \frac{(\lambda_{m1} + 3\lambda_{m3} \cdot k_{13} + 5\lambda_{m5} \cdot k_{15}) \cdot \sqrt{2} I_{RMS}}{\sqrt{1 + k_{13}^2 + k_{15}^2}} \quad (11)$$

Expressions (9)-(11) are particular cases of the general case, for which the equations are given in the Appendix.

Apart from I_{RMS} (which is for simplicity taken as $1/\sqrt{2}$ A) and constants n , P , λ_{m1} , λ_{m3} and λ_{m5} , there are in (11) three variables (k_{13} , k_{15} , T_{em}). By solving this three-dimensional function, the plot presented in Fig. 9 is obtained. The corresponding results are summarised in Table III (the first three rows). The maximal electromagnetic torque, achievable with both injected harmonics, is $T_{emmax} = 2.52$ Nm. To achieve such torque, calculated optimal harmonic current injection ratios must be $k_{13opt} = 0.927$ and $k_{15opt} = 0.497$.

If compared with the results obtained with only third harmonic injection [24], it follows that the value of the optimal injection ratio k_{13opt} stays unchanged. The corresponding FE analysis results, discussed in Section II-B, are included in the last column of the Table III. As can be seen, FE results are in good agreement with the analytical ones.

By including the seventh harmonic into the maximal achievable torque calculation, (3), (7)-(8) get slightly modified and the results shown in the last row of the Table III are obtained. Because there are now four variables (k_{13} , k_{15} , k_{17} , T_{em}), a plot cannot be produced. Contribution of the 7th harmonic to the total torque is here negligible; hence this harmonic is not used further on.

The complexity of the system to be solved increases by one dimension with every additional harmonic used for the torque improvement. However, optimal harmonic current injection ratios do not change when new harmonics are injected. This leads to the conclusion that optimal ratios can be calculated separately by solving the less complex 2D functions:

$$\begin{aligned} T_{em13} &= \frac{n \cdot P}{2} \cdot \frac{(\lambda_{m1} + 3 \cdot \lambda_{m3} \cdot k_{13}) \cdot \sqrt{2} I_{RMS}}{\sqrt{1 + k_{13}^2}} \rightarrow \text{for } 1^{st} + 3^{rd} \\ T_{em15} &= \frac{n \cdot P}{2} \cdot \frac{(\lambda_{m1} + 5 \cdot \lambda_{m5} \cdot k_{15}) \cdot \sqrt{2} I_{RMS}}{\sqrt{1 + k_{15}^2}} \rightarrow \text{for } 1^{st} + 5^{th} \\ T_{em17} &= \frac{n \cdot P}{2} \cdot \frac{(\lambda_{m1} + 7 \cdot \lambda_{m7} \cdot k_{17}) \cdot \sqrt{2} I_{RMS}}{\sqrt{1 + k_{17}^2}} \rightarrow \text{for } 1^{st} + 7^{th} \end{aligned} \quad (12)$$

To confirm this, results recorded after solving three two-dimensional functions (12) are shown in Fig. 10. The same values of the coefficients are obtained as before when one multi-dimensional system was solved (Fig. 9, Table III). Although being easier to execute, the 2D method does not provide final achievable torque value immediately. By using the optimal ratios from 2D analysis and I_{RMS} , maximal electromagnetic torque can be calculated as:

$$T_{emmax} = \frac{n \cdot P}{2} \left(\lambda_{m1} + \sum_{l=1}^l h(l) \lambda_{mh(l)} k_{1h(l)} \right) \cdot \frac{\sqrt{2} I_{RMS}}{\sqrt{1 + \sum_{l=1}^l k_{1h(l)}^2}} \quad (13)$$

where $h = [3, 5, \dots, n-2]$ and $l = [(n-3)/2]$.

By applying MTPA principle for multi-dimensional injection ratio calculations, optimal h^{th} harmonic injection ratio calculation can be defined as:

$$k_{1hopt} = \frac{h \cdot \lambda_{mh}}{\lambda_{m1}} = \frac{e_h}{e_1} \quad (14)$$

In Table IV calculated torque values from Table III are reproduced and achievable torque improvements are calculated. The third-harmonic current injection increases the torque by $\approx 36\%$ [24]. Adding further the fifth harmonic, the maximal torque becomes 2.52 Nm, which is $\approx 45\%$ improvement with respect to the torque produced by the fundamental only. That is, an additional $\approx 6\%$ improvement is achieved with respect to the third harmonic injection. Finally, after the seventh harmonic is also employed, maximal torque value is 2.53 Nm. Hence the final maximum achievable torque with injection of all possible harmonics is 45.40% higher than the torque produced only with the fundamental harmonic. If compared with the improvement obtainable with the combined third and fifth harmonic components, new value is only around 0.4% higher. Hence, the seventh harmonic is not used and resonant (VPI) controller forces the currents of the second plane to zero.

V. POSITION-SENSORLESS CONTROL

As noted already, the idea is to utilise existence of one of the back-EMF harmonics for estimation of the rotor position and thus realise continued drive operation in the case of the position sensor failure. The basics of the technique have been

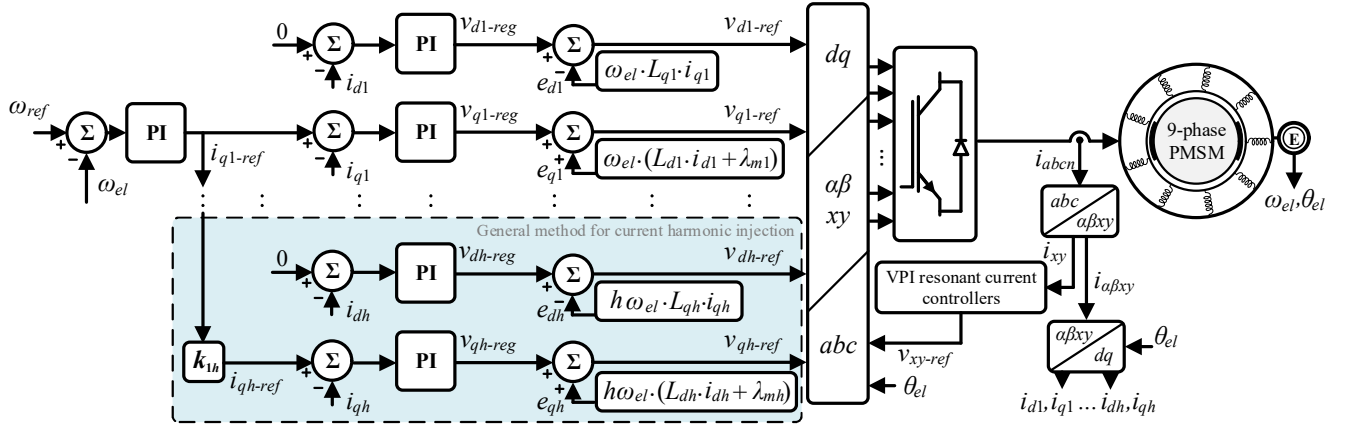


Fig. 8. Field-oriented control algorithm modified for general harmonic current injection and low-order harmonic elimination.

TABLE III. OPTIMAL INJECTION RATIOS AND TORQUE VALUES FOR THE USE OF THE 1st, 3rd, 5th AND 7th HARMONICS.

Harmonics	k_{opt}	T_{emmax} [Nm]	FE T_{emmax} [Nm]
1 st	$k_1 = 1$	1.74	1.68
1 st + 3 rd	$k_{13} = 0.927$	2.38	2.24
1 st , 3 rd + 5 th	$k_{15} = 0.497$	2.52	2.39
1 st , 3 rd , 5 th + 7 th	$k_{17} = 0.128$	2.53	2.41

TABLE IV. ELECTROMAGNETIC TORQUE IMPROVEMENT ANALYSIS.

Harmonics Injected	T_{em} [Nm]	Imp. from only 1 st	Imp. from 1 st and 3 rd	Imp. from 1 st , 3 rd & 5 th
1 st	1.74			
1 st + 3 rd	2.38	36.21%		
1 st , 3 rd + 5 th	2.52	44.83%	6.33%	
1 st , 3 rd , 5 th + 7 th	2.53	45.40%	6.75%	0.4%

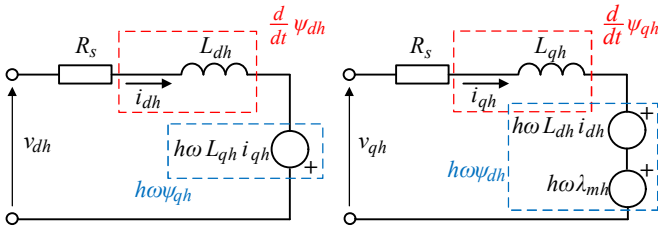


Fig. 7. Generalized equivalent d-q electrical circuits for a PMSM.

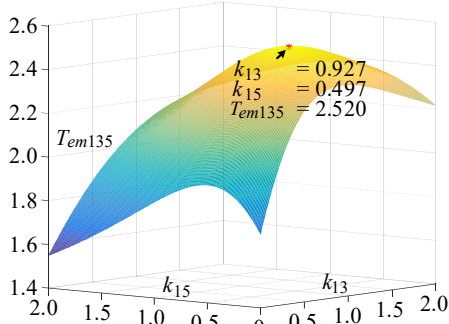


Fig. 9. 3D torque plot against current harmonic injection ratios (added indices in torque symbols specify which harmonics are injected).

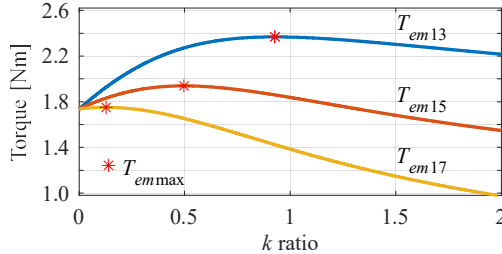


Fig. 10. Torque versus injection ratio with a single harmonic injection (added indices in torque symbols specify which harmonics are injected).

introduced in [27], where position sensorless control utilised the third back-EMF harmonic. There are two possible scenarios: in the first one a selected plane is not used for torque enhancement at all (as in [27]), while in the second case the plane is used for

torque enhancement as long as the position sensor is in healthy state. In both cases the sole purpose of the selected plane/harmonic is to enable rotor position estimation once when the position sensor failure is detected.

The difference in the two scenarios stems from the fact that the back-EMF of any particular plane cannot be sensed and only x-y voltages, applied as references, are known. In the former case there is no current flow in the given plane prior to sensor fault and the back-EMF equals stator x-y voltages (regarded as equal to the reference values; dead time and on-state voltage drop are neglected). In the latter case, the applied x-y voltages differ from the back-EMF because of the harmonic current flow prior to the sensor failure. The latter case, in line with the developments of the previous section, is considered further on.

Since the considered machine has sufficiently high values of the third and the fifth back-EMF harmonics, these two harmonics are used initially for the torque enhancement. At the instant of position sensor fault detection, the fifth back-EMF harmonic becomes a medium used for rotor position estimation, so that the torque enhancement further on relies on the third stator current harmonic injection (in the third x-y plane) only. Machine model, which takes into account back-EMF harmonics of the order 1 to 7, after VSD transformation and using complex space vector notation (underlined variables), is given with:

$$\begin{cases} \underline{v}_{\alpha\beta} = R_s \cdot \underline{i}_{\alpha\beta} + L_1 \cdot \frac{d\underline{i}_{\alpha\beta}}{dt} + j\omega\lambda_{m1} \cdot e^{-j(\theta_{el} + \theta_1)} \\ \underline{v}_{xy1} = R_s \cdot \underline{i}_{xy1} + L_7 \cdot \frac{d\underline{i}_{xy1}}{dt} - j7\omega\lambda_{m7} \cdot e^{-j(7\theta_{el} + \theta_7)} \\ \underline{v}_{xy2} = R_s \cdot \underline{i}_{xy2} + L_5 \cdot \frac{d\underline{i}_{xy2}}{dt} - j5\omega\lambda_{m5} \cdot e^{-j(5\theta_{el} + \theta_5)} \\ \underline{v}_{xy3} = R_s \cdot \underline{i}_{xy3} + L_3 \cdot \frac{d\underline{i}_{xy3}}{dt} + j3\omega\lambda_{m3} \cdot e^{-j(3\theta_{el} + \theta_3)} \end{cases} \quad (15)$$

The relevant equation is the one for the x_2 - y_2 plane. Since the fifth harmonic is initially used for torque boosting, the fifth harmonic current reference gets instantaneously reduced to zero

when position sensor failure is detected, so that the voltage equation becomes:

$$\underline{v}_{xy2} = \hat{\underline{e}}_{xy2} = -j5\omega \cdot \lambda_{m5} \cdot e^{-j5\theta_{el}} \quad (16)$$

where the initial phase of the fifth harmonic back-EMF is taken as zero on the basis of Fig. 2 and $\hat{\cdot}$ stands for an estimated value. The argument of the back-EMF in (16) contains rotor position information. It can be obtained after reconstruction of the phase voltage references generated at the output of the control system,

$$5\hat{\theta}_{el} = \arctan\left(\frac{\sin(5 \cdot \hat{\theta}_{el})}{\cos(5 \cdot \hat{\theta}_{el})}\right) = \arctan\left(\frac{-\hat{e}_{x5}}{-\hat{e}_{y5}}\right) \quad (17)$$

$$\sin(5 \cdot \hat{\theta}_{el}) = \frac{-\hat{e}_{x5}}{\sqrt{\hat{e}_{x5}^2 + \hat{e}_{y5}^2}}; \quad \cos(5 \cdot \hat{\theta}_{el}) = \frac{-\hat{e}_{y5}}{\sqrt{\hat{e}_{x5}^2 + \hat{e}_{y5}^2}} \quad (18)$$

Since finding inverse of trigonometric functions is computationally intensive, rotor position and speed information are obtained using a phase-locked-loop (PLL) [27], [29], shown in Fig. 11. It receives at the input voltage reference $\underline{v}_{xy2-ref}$ reconstructed from the FOC algorithm, while on its output it provides angle information θ_{PLL} , from which rotor position can be extracted. PLL error ε_θ can be approximated, assuming that is it small, with [30]:

$$\begin{aligned} \varepsilon_\theta &\approx \sin(5\hat{\theta}_{el} - \theta_{PLL}) \\ &\approx \sin(5\hat{\theta}_{el}) \cdot \cos(\theta_{PLL}) - \cos(5\hat{\theta}_{el}) \cdot \sin(\theta_{PLL}) \end{aligned} \quad (19)$$

The error is then forwarded to the input of the PI controller, which gives at the output estimated speed ω_{PLL} ; it can be used directly as a feedback of the speed control loop in the sensorless control mode. To obtain feedback angle θ_{PLL} , the estimated speed is integrated. Because of the harmonic gain (equal to 5) in the feedback loop, θ_{PLL} angle is actually equal to the estimated rotor position (i.e. electrical angle $\hat{\theta}_{el}$).

The control scheme of Fig. 8 is for sensorless control modified in the part associated with the 5th harmonic of the back-EMF, which now has the form illustrated in Fig. 12.

VI. EXPERIMENTAL VALIDATION

A. Experimental Rig

An experimental rig, shown in Fig. 13, is used. The shaft of the machine is coupled to a dc machine by a Datum Electronics M425 torque meter. Dc machine Leeson 108371 is PM excited, rated at 1.1/1.5 kW, 180 V, 9 A, 1800 rpm and is connected to a resistor bank for loading purposes. The PMSM is supplied using two custom-made inverters, based on Infineon FS50R12KE3 IGBT modules. The inverters have hardware-implemented dead time of 6 μ s. Inverter dc-link voltage (450 V) is provided by Sorensen SG1600/25 single-quadrant dc-voltage source. Measurement and control are realized by rapid prototyping platform dSPACE. An ADC board is used to acquire phase currents measured by inverter's internal LEM sensors, while an incremental encoder board provides speed and position. Additional measurements are taken using Tektronix DPO/MSO 2014 oscilloscopes, equipped with current probes (TCP0030A) and high-voltage differential probes (P5205A).

B. Torque Enhancement

Steady state operation is examined first. Recorded sequence has three segments and its total duration is 6 s. In the first 2 s only fundamental current is used for torque production ($k_{13} = k_{15} = 0$). In the next 2 s (1st + 3rd harmonic region), injection ratio k_{13} is changed to its optimal value $k_{13} = 0.93$ ($k_{15} = 0$), while in the last 2 s (1st, 3rd + 5th harmonic region), in

addition to the third, the fifth harmonic current injection is also employed for torque production ($k_{15} = 0.5$). The machine runs at 1500 rpm and the load torque is kept the same throughout, while the phase current RMS changes. This approach is used since, to replicate numerical results of Table IV, one would need a continuously variable resistor for connection to the dc generator armature (which is not available). From the point of view of verifying the results of Table IV, the used approach simply comes down to the expectation that the reduction in the current RMS will be similar/the same as the corresponding torque increase in the table.

Measured phase currents can be seen in Fig. 14. Entire sequence is shown first (upper plot; phase $a1$), followed by the transient intervals (middle plots; phases $a1$, $a2$, $a3$). Transient time is of 0.2 s duration. The phase current peak value increases with addition of harmonics. Its value is 1.16 A for the fundamental only, 1.23 A for the 1st and 3rd harmonic, and 1.34 A for the 1st, 3rd and 5th harmonic. The phase current RMS value, however, decreases. In the 1st + 3rd harmonic region, it is 0.60 A, i.e. lower than the one in the first region (0.82 A). Percentage decrease in RMS current is, as expected, $\approx 36\%$ lower [24]. In the 1st, 3rd + 5th harmonic region where the fifth harmonic is also used, phase current RMS value is 0.56 A, i.e. approximately 45% lower than the value calculated for fundamental only, and approximately 6% lower with the respect to the 1st + 3rd harmonic current injection case. Measured phase $a1$ current harmonic spectrum for each region is also given in Fig. 14 (bottom plots). The calculated phase current reduction results are in a good agreement with the torque improvement results obtained mathematically (Table IV).

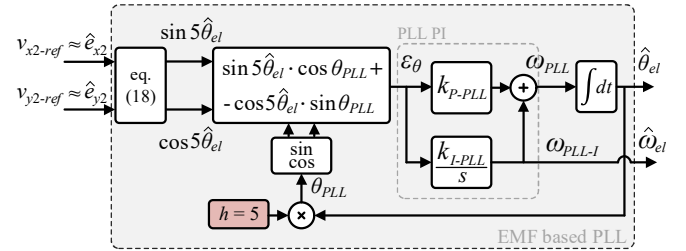


Fig. 11. Back-EMF based phase-locked-loop.

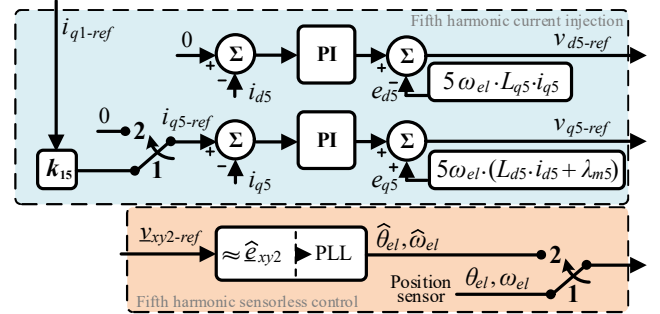


Fig. 12. Implementation of the fifth harmonic use for torque enhancement and for sensorless position estimation.

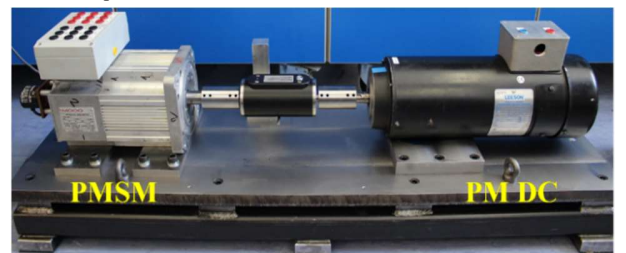


Fig. 13. Experimental rig.

Filtered phase voltage waveforms can be seen in Fig. 15. Two intervals around transition instants (the same as in Fig. 14) are shown. Non-sinusoidal shape of phase voltage is directly related to the non-sinusoidal back-EMF to which additional voltages from controllers are added to zero or to control (as applicable) induced current harmonic components.

In Fig. 16 power results are shown. To obtain the traces in Fig. 16, the voltage and current of the first phase in each three-phase set are measured using current and voltage probes and the two synchronised oscilloscopes. The values are then imported into Matlab. It is assumed that power per-phase in each three-phase set is the same, and input power is then calculated through voltage and current multiplication. To get the stator winding loss, RMS of the measured current in the first phase of each three-phase set is calculated using Matlab. It is assumed that the same value applies to all three phases, and scaling with the stator resistance of Table I is done.

Because speed and torque are constant during the entire testing sequence, output power is constant as well. Input power of the machine however decreases each time when an additional current harmonic is injected. This can be directly related to the reduced phase current RMS value. Calculated stator copper

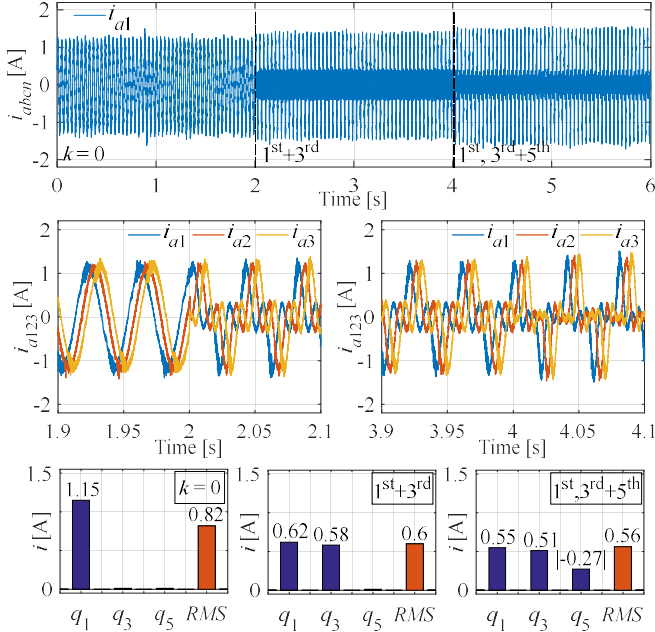


Fig. 14. Phase currents and corresponding (phase a1) harmonic spectra.

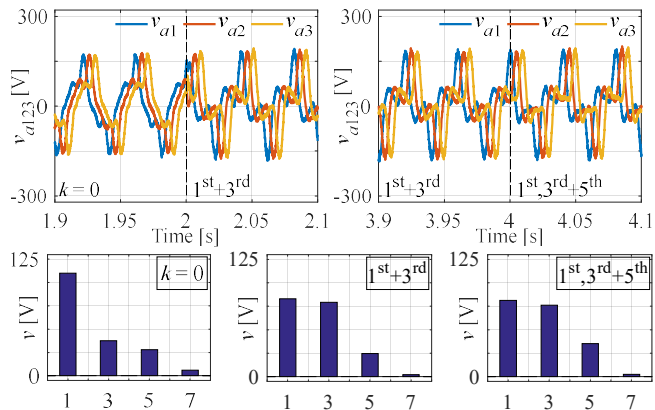


Fig. 15. Phase voltages around transition points (filtered oscilloscope traces; 2.9 kHz filter was used) and corresponding (phase a1) harmonic spectra.

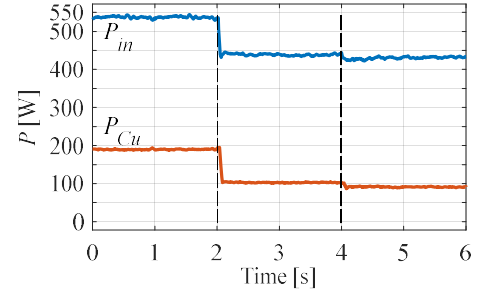


Fig. 16. Input power and stator winding losses.

losses recorded with injected third plus fifth harmonic are approximately 100 W lower than in the fundamental case only. This once again confirms electromagnetic torque improvement analysis because calculated ratio between phase current RMS values is $\sqrt{P_{Cu1} / P_{Cu135}} = I_{RMS1} / I_{RMS135} = 1.451 (\approx 45\%)$.

Current mapping after VSD can be seen in Fig. 17a. In 0-2 s region, only fundamental component is used and hence only α - β currents exist. In the second region (2-4 s), the third-harmonic current injection is employed resulting in additional x - y current components in the x_3 - y_3 subspace. As x_3 - y_3 currents increase, peak values of α - β currents decrease. Similar response can be observed also in the last region (4-6 s) where the fifth harmonic is injected as well, so that the other components decrease. Flux- and torque-producing currents in multiple synchronous frames (Fig. 17b), obtained from measured currents and known rotor position, confirm the above given statements. Exact values of each torque producing current in different regions are summarised in Table V. It is important to note that the fifth harmonic rotates in the anti-synchronous direction. Hence, the only way to obtain constant x - y voltage references at the output of the PI is to perform a rotation in the backward (anti-synchronous) direction using the inverse Park's transformation first [31]. As a consequence, i_{q5} is negative. During the entire sequence, all three flux-producing currents (i_{d1} , i_{d3} , i_{d5}) are controlled and equal to zero (MTPA).

Next, the machine's performance is tested in transient operation. The results in Fig. 18 show measured speed and phase currents. The machine is started at $t = 0.2$ s with i) fundamental current only, ii) 1st + 3rd and iii) 1st + 3rd + 5th current harmonics. Load torque setting is the same for all three cases and speed reference is returned to zero at $t = 3$ s. The results show that speed response is faster when current harmonic injection is used, since a higher torque can be developed for any given stator current RMS limiting value. The difference between the speed transients with the 3rd and the 3rd + 5th harmonic is rather small and not observable in the traces.

C. Sensorless Operation

Prior to the assumed position sensor fault the machine operates with the torque produced by the fundamental, the 3rd and the 5th harmonic. At the instant of sensor fault the switch positions in Fig. 12 are instantaneously changed from 1 to 2 in the software, so that the output of Fig. 11 is used further on as the estimated rotor position. This means that the fifth harmonic current reference is stepped from previous value to zero. Prior to this switch position change voltage reference in the relevant plane was not equal to the back-EMF. Hence, a transient is inevitable as there is an initial position estimation error.

Prior to the fault, the machine operates in steady state at 1000 rpm with a load torque of app. 0.87 Nm. The position tracking runs in the background and the fault happens at the

instant $t = 0.08$ s. Speed response is shown in Fig. 19, while Fig. 20 shows corresponding oscilloscope screenshot of currents and measured torque. It can be seen from the current waveforms that, at the instant of fault, the current shape changes, since the fifth harmonic is zeroed. Torque trace clearly indicates that there is an unwanted transient although the load torque has not changed and this is visible from the speed traces as well. Fig. 21 illustrates actual and estimated position, as well as the position estimation error. The transients in the torque and speed are the consequence of the error in the estimated position, which is during the healthy operation app. 10° .

Once when the post-fault operation has taken place the error reduces to app. 6° , and speed and torque return to pre-fault values. Similar final position estimation error in post-fault operation results if the 5th harmonic is not used for torque enhancement prior to the fault; in such a case however the transients visible in Figs. 19-20 do not take place.

TABLE V. TORQUE-PRODUCING CURRENTS ANALYSIS.

i_{qh} [A]	$k = 0$	$1^{st} + 3^{rd}$	$1^{st}, 3^{rd} + 5^{th}$
i_{q1}	1.1549	0.6207	0.5484
i_{q3}	0	0.5772	0.5086
i_{q5}	0	0	-0.2743

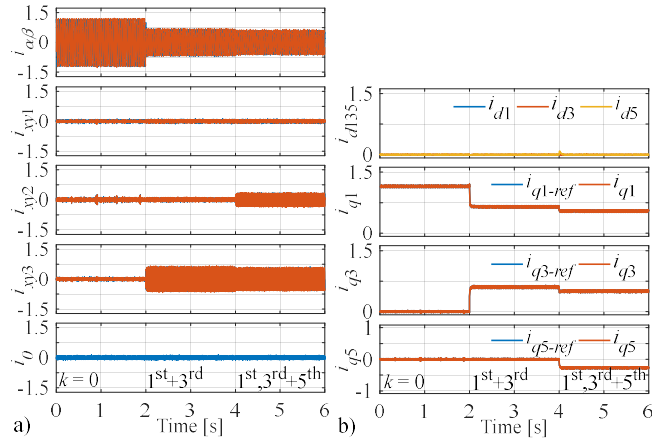


Fig. 17. α - β (a) and rotational domain (b) currents.

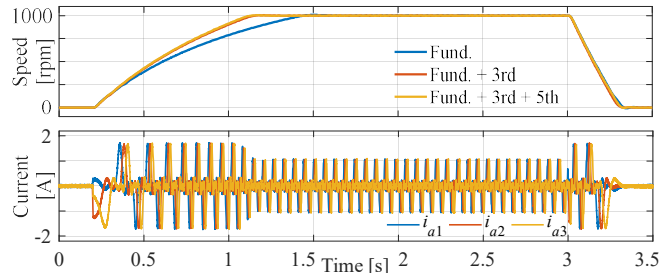


Fig. 18. Machine's transient performance during acceleration and deceleration.

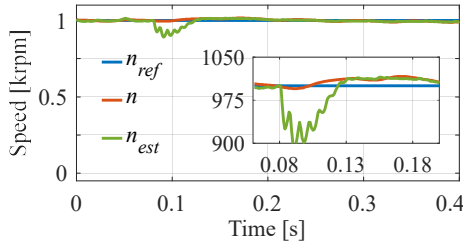


Fig. 19. Experimentally recorded speeds (position sensor fault takes place at 0.08 s in steady state at 1000 rpm).

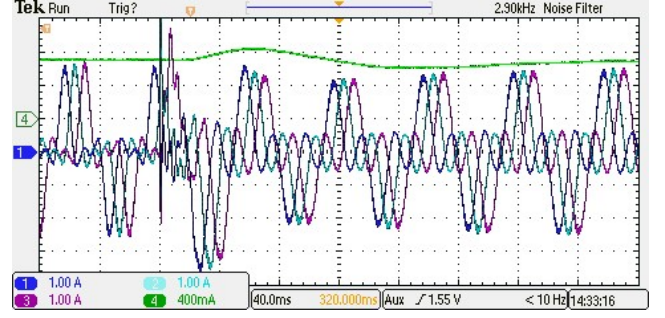


Fig. 20. Oscilloscope screenshot of phase currents (phases $a1$, $a2$, $a3$; 1 A on oscilloscope = 0.25 A of real current) and electromagnetic torque measured with torque meter (400 mA = 0.5 Nm of real torque). Waveforms filtered with a 2.9 kHz filter.

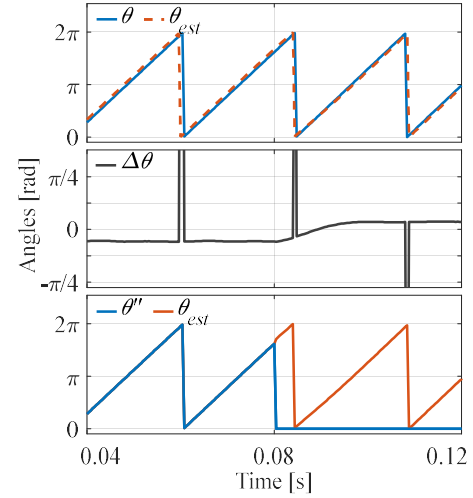


Fig. 21. Position angle analysis: actual and estimated angles and position estimation error (zoomed extracts around the instant of fault; θ'' stands for encoder position signal θ as seen by the control system).

Introduced fault tolerant operation works satisfactorily in both the steady states and transients, as shown next. Effective changeover is achieved at speeds above 250 rpm, i.e. roughly above 10% of the rated speed. In the test, the loaded machine is accelerated from 0 to 1000 rpm reference speed using a ramp. The sensor fault is emulated at 500 rpm. Behaviour of the drive is shown in Figs. 22 (speeds), 23 (currents and measured torque) and 24 (rotor position related signals).

There is again an unwanted transient in speed and torque responses at the instant of fault. However, the control rather quickly overcomes the disturbance and the drive continues to operate in position sensorless mode without stability problems.

As noted above, undesirable transients, visible in Figs. 19-20 and 22-23, appear because of the initial use of the fifth stator current harmonic for torque boosting. They practically disappear if the torque boosting with the fifth harmonic is not used and the fifth harmonic is continuously used for rotor position tracking purposes. The same transient, already shown in Figs. 22-23, is illustrated again in Figs. 25-26 – but, here the fifth harmonic is not used prior to the sensor fault for torque enhancement. As can be seen, the changeover to sensorless mode is now almost seamless.

The last studied case is a transient that follows step loading of the machine during operation in sensorless mode (post-fault operation) in steady state at 1200 rpm, from no-load condition. Experimentally recorded estimated speed (used for control) and

actual speed (recorded for display purposes only), as well as stator currents, are given in Fig. 27. As can be seen, the disturbance rejection transient is stable and there are not any problems associated with the sensorless mode of operation.

VII. CONCLUSION

A nine-phase surface PMSM with reduced PM content is studied in the paper. It is shown that in a machine with reduced magnet span developed torque can be significantly enhanced by injecting low-order stator current harmonics. A field-oriented control algorithm is further devised using the MTPA principles and operation of the machine is tested using injection of different harmonics. In the prototype machine with 45° magnet span $\approx 45\%$ higher output torque is achieved when all the harmonics are injected than just with the fundamental. Simultaneously, the current RMS is reduced, leading to a

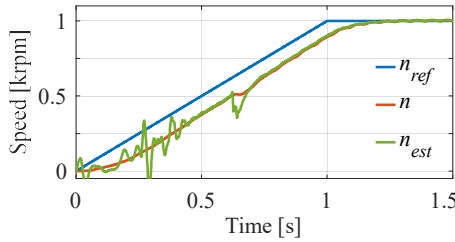


Fig. 22. Acceleration from 0 to 1000 rpm with the sensor fault taking place at 500 rpm.

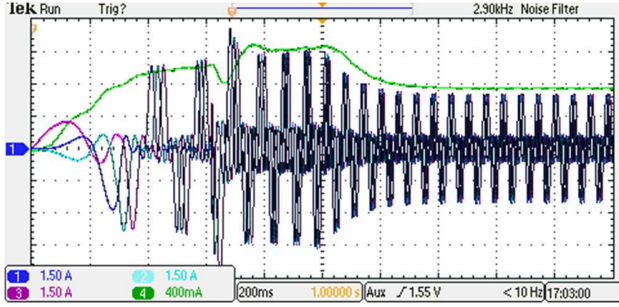


Fig. 23. Acceleration from zero to 1000 with sensor fault at 500 rpm: phase currents (phases a_1 , a_2 , a_3 ; 1.5 A on oscilloscope = 0.375 A of real current) and electromagnetic torque measured with torque meter (400 mA = 0.5 Nm of real torque). Waveforms filtered with a 2.9 kHz filter.

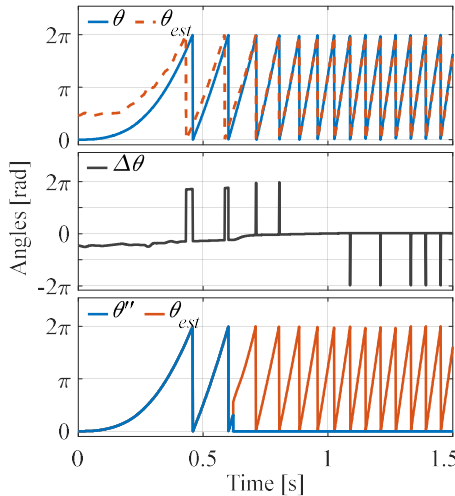


Fig. 24. Acceleration from 0 to 1000 rpm with sensor fault at 500 rpm: analysis: actual and estimated angles and position estimation error (θ'' stands for encoder position signal θ as seen by the control system).

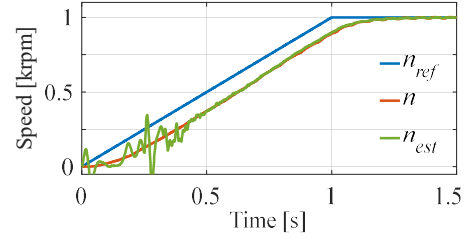


Fig. 25. Acceleration from 0 to 1000 rpm with the sensor fault taking place at 500 rpm. The fifth stator current harmonic injection is not used for torque boosting in healthy operation prior to the sensor fault instant.

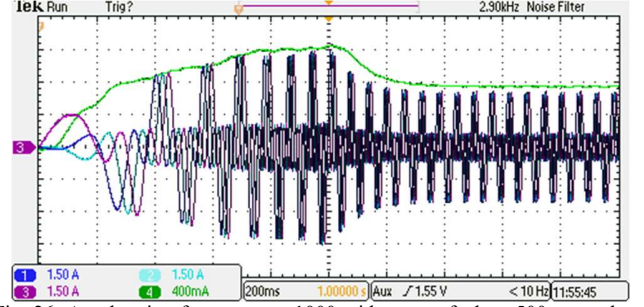


Fig. 26. Acceleration from zero to 1000 with sensor fault at 500 rpm: phase currents (phases a_1 , a_2 , a_3 ; 1.5 A on oscilloscope = 0.375 A of real current) and electromagnetic torque measured with torque meter (400 mA = 0.5 Nm of real torque). Waveforms filtered with a 2.9 kHz filter. The fifth stator current harmonic injection is not used for torque boosting in healthy operation prior to the sensor fault instant.

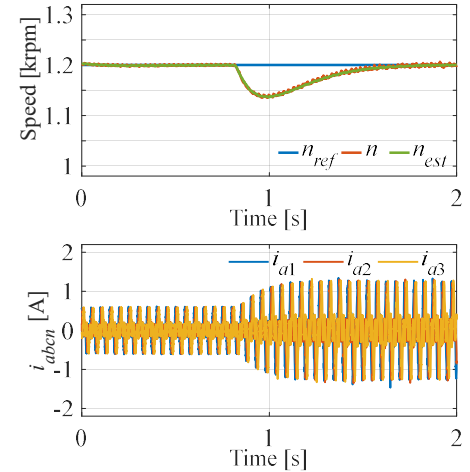


Fig. 27. Experimentally recorded speeds (top) and phase currents (bottom) during step load torque change transient at 1200 rpm.

decrease in the machine's losses. An important conclusion is that a machine with optimal magnet span of around 70° would be able to develop insignificantly lower torque than the machine with full 180° span.

Next, back-EMF harmonic based rotor position estimation is introduced in order to achieve position sensor fault tolerance. At the instant of fault, torque enhancement in one plane is replaced with the use of the back-EMF harmonic to estimate the rotor position. The changeover is illustrated experimentally in both steady state and transient operation of the drive and is applicable at speeds above roughly 0.1 per-unit.

Further directions for research include an investigation of the impact of the position estimation error in sensorless mode on the drive performance, as well as a study of the linear PWM region limits for the specific machine design developed here. It is expected that the specific back-EMF shape may adversely

affect dc-bus voltage utilisation in the liner PWM region. Last but not least, behaviour of the drive in sensorless mode during open-phase faults appears to be a worthy further stream of investigation.

APPENDIX: GENERAL FORM OF (9)-(11)

In a general case, for injection of any number of harmonics, expressions (9)-(11) can be written as:

$$T_{em} = \frac{n \cdot P}{2} \cdot (\lambda_{m1} i_{q1} + \dots + h \lambda_{mh} i_{qh}) \quad (20)$$

$$k_{1h} = \frac{i_{qh}}{i_{q1}} \rightarrow T_{em} = \frac{n \cdot P}{2} \cdot (\lambda_{m1} + \dots + h \lambda_{mh} k_{1h}) \cdot i_{q1}$$

$$I_{RMS} = \sqrt{(i_{q1}^2 + \dots + i_{qh}^2) / 2} \rightarrow i_{q1} = \frac{\sqrt{2} I_{RMS}}{\sqrt{(1 + \dots + k_{1h}^2)}} \quad (21)$$

$$T_{em} = \frac{nP}{2} \cdot \frac{(\lambda_{m1} + \dots + h \lambda_{mh} \cdot k_{1h}) \cdot \sqrt{2} I_{RMS}}{\sqrt{1 + \dots + k_{1h}^2}} \quad (22)$$

REFERENCES

- [1] B. Aslan, E. Semail, "New 5-phase concentrated winding machine with bi-harmonic rotor for automotive application," *Int. Conf. Electrical Machines ICEM*, pp. 2114-2119, 2014.
- [2] M. Onsal, Y. Demir and M. Aydin, "A new nine-phase permanent magnet synchronous motor with consequent pole rotor for high-power traction applications," *IEEE Trans. Magnetics*, vol. 53, no. 11, pp. 1-6, 2017.
- [3] F. Sculler, H. Zahr and E. Semail, "A bi-harmonic five-phase SPM machine with low ripple torque for marine propulsion," *IEEE Int. Electric Machines and Drives Conf. IEMDC*, pp. 1-7, 2017.
- [4] X. Huang, A. Goodman, C. Gerada, Y. Fang and Q. Lu, "Design of a five-phase brushless DC motor for a safety critical aerospace application," *IEEE Trans. Ind. Electron.*, vol. 59, no. 9, pp. 3532-3541, 2012.
- [5] P. J. McCleer, J. M. Bailey, J. S. Lawler and B. Banerjee, "Five phase trapezoidal back emf PM synchronous machines and drives," *Eur. Power Electron. and Appl. Conf. EPE*, pp. 128-133, 1991.
- [6] L. Parsa, H. A. Toliyat, "Five-phase permanent magnet motor drives," *IEEE Trans. Ind. Appl.*, vol. 41, no. 1, pp. 30-37, 2005.
- [7] F. Sculler, E. Semail, J.-F. Charpentier and P. Letellier, "Multi-criteria-based design approach of multi-phase permanent magnet low-speed synchronous machines," *IET Electr. Power Appl.* vol. 3, no. 2, pp. 102-110, 2009.
- [8] K. Wang, Z. Q. Zhu, G. Ombach, "Torque enhancement of surface mounted permanent magnet machine using third-order harmonic," *IEEE Trans. Mag.*, vol. 50, no. 3, pp. 104-113, 2014.
- [9] H. Zahr, E. Semail, B. Aslan and F. Sculler, "Maximum torque per Ampere strategy for a biharmonic five-phase synchronous machine," *Int. Sym. on Power Electronics, Electrical Drives, Automation and Motion SPEEDAM*, pp. 91-97, 2016.
- [10] J. Gong, H. Zahr, E. Semail, M. Trabelsi, B. Aslan and F. Sculler, "Design considerations of five-phase machine with double p/3p polarity," *IEEE Trans. Energy Conv.*, vol. 34, no. 1, pp. 12-24, 2019.
- [11] Z. Q. Zhu, K. Wang and G. Ombach, "Optimal magnet shaping with third order harmonic for maximum torque in SPM machines," *6th IET Conf. on Power Electron., Mach. and Drives*, pp. 1-6, 2012.
- [12] K. Wang, Z. Y. Gu, Z. Q. Zhu and Z. Z. Wu, "Optimum injected harmonics into magnet shape in multiphase surface-mounted PM machine for maximum output torque," *IEEE Trans. on Ind. Electron.*, vol. 64, no. 6, pp. 4434-4443, 2017.
- [13] K. Wang, Z. Y. Gu, C. Liu and Z. Q. Zhu, "Design and analysis of a five-phase SPM machine considering third harmonic current injection," *IEEE Trans. Energy Conv.*, vol. 33, no. 3, pp. 1108-1117, 2018.
- [14] Z. Y. Gu, K. Wang, Z. Q. Zhu, Z. Z. Wu, C. Liu and R. W. Cao, "Torque improvement in five-phase unequal tooth SPM machine by injecting third harmonic current," *IEEE Trans. Vehicular Technology*, vol. 67, no. 1, pp. 206-215, 2018.
- [15] L. F. Zhang, K. Wang, H. Y. Sun and S. S. Zhu, "Multiphase PM machines with Halbach array considering third harmonic flux density," *IEEE Trans. Ind. Electron.*, vol. 66, no. 12, pp. 9184-9193, 2019.
- [16] Y. Sui, P. Zheng, Y. Fan and J. Zhao, "Research on the vector control strategy of five-phase PMSM based on third-harmonic current injection," *IEEE Int. Electric Machines and Drives Conf.*, pp. 1-8, 2017.
- [17] X. Kestelyn and E. Semail, "A vectorial approach for generation of optimal current references for multiphase permanent-magnet synchronous machines in real time," *IEEE Trans. Ind. Electron.*, vol. 58, no. 11, pp. 5057-5065, 2011.
- [18] Y. Hu, Z. Q. Zhu and K. Liu, "Current control for dual three-phase permanent magnet synchronous motors accounting for current unbalance and harmonics," *IEEE J. Emerg. Sel. Top. Power Electron.*, vol. 2, no. 2, pp. 272-284, 2014.
- [19] Y. Hu, Z. Q. Zhu and M. Odavic, "Torque capability enhancement of dual three-phase PMSM drive with fifth and seventh current harmonics injection," *IEEE Trans. Ind. Appl.*, vol. 53, no. 5, pp. 4526-4535, 2017.
- [20] H. Zhang, B. Zhao, J. Gong, Y. Xu, D. T. Vu, N. K. Nguyen, E. Semail and T. J. dos S. Moraes, "Torque optimization of a seven-phase bi-harmonic PMSM in healthy and degraded Mode," *Int. Conf. on Electrical Machines and Systems ICEMS*, pp. 1-6, 2019.
- [21] F. Locment, E. Semail and X. Kestelyn, "Vectorial approach-based control of a seven-phase axial flux machine designed for fault operation," *IEEE Trans. Ind. Electron.* vol. 55, no. 10, pp. 3682-3691, 2008.
- [22] M. Farshadnia, M. A. M. Cheema, A. Pouramin, R. Dutta and J. E. Fletcher, "Design of optimal winding configurations for symmetrical multiphase concentrated-wound surface-mount PMSMs to achieve maximum torque density under current harmonic injection," *IEEE Trans. Ind. Electron.*, vol. 65, no. 2, pp. 1751-1761, 2018.
- [23] A. Gautam, S. Karugaba and J. Ojo, "Modeling of nine-phase interior permanent magnet machines (IPM) including harmonic effects," *IEEE Int. Electric Machines and Drives Conf.*, pp. 681-686, 2011.
- [24] M. Slunjski, M. Jones and E. Levi, "Control of a symmetrical nine-phase PMSM with highly non-sinusoidal back-electromotive force using third harmonic current injection," *Ann. Conf. of IEEE Ind. Electron. Soc. IECON*, pp. 969-974, 2019.
- [25] S. Chung, J. Kim, Y. Chun, B. Woo and D. Hong, "Fractional slot concentrated winding PMSM with consequent pole rotor for a low-speed direct drive: Reduction of rare earth permanent magnet," *IEEE Trans. Energy Con.*, vol. 30, no. 1, pp. 103-109, 2015.
- [26] M. Slunjski, M. Jones and E. Levi, "Analysis of a symmetrical nine-phase machine with highly non-sinusoidal back-EMF force," *Ann. Conf. of IEEE Ind. Electron. Soc. IECON*, pp. 6229-6234, 2018.
- [27] O. Stiscia, M. Slunjski, E. Levi and A. Cavagnino, "Sensorless control of a nine-phase surface mounted permanent magnet synchronous machine with highly non-sinusoidal back-EMF," *Ann. Conf. of IEEE Ind. Electron. Soc. IECON*, pp. 1327-1332, 2019.
- [28] A. G. Yepes, J. Doval-Gandoy, F. Baneira, D. Pérez-Estévez and O. López, "Current harmonic compensation for n -phase machines with asymmetrical winding arrangement and different neutral configurations," *IEEE Trans. Ind. Appl.*, vol. 53, no. 6, pp. 5426-5439, 2017.
- [29] F. De Belie, X. Kestelyn and N. K. Nguyen, "Fault-tolerant optimal-current torque-controlled five-phase PMSMs with open-circuited phases: Position self-sensing operation," *IEEE Vehicle Power and Propulsion Conf. VPP*, pp. 1-6, 2014.
- [30] S. Bolognani, S. Calligaro and R. Petrella, "Design issues and estimation errors analysis of back-EMF-based position and speed observer for SPM synchronous motors," *IEEE J. Emerg. Sel. Topics Power Electron.*, vol. 2, no. 2, pp. 159-170, 2014.
- [31] I. Gonzalez-Prieto, M. J. Duran, H. S. Che, E. Levi, M. Bermúdez, F. Barrero, "Fault-tolerant operation of six-phase energy conversion systems with parallel machine-side converters," *IEEE Trans. Pow. Electron.*, vol. 31, no. 4, pp. 3068-3079, 2016.



Marko Slunjski (S'18) received the BSc and MSc degrees in Electrical Engineering from the University of Zagreb, Faculty of Electrical Engineering and Computing, Croatia in 2015 and 2017, respectively. Since July 2017, he has been with Liverpool John Moores University, Liverpool, U.K., where he is working toward the Ph.D. degree in electrical engineering. His main research interests are in the areas of power electronics and advanced variable speed multiphase drive systems.



Ornella Stiscia (S'19) received the B.Sc. and M.Sc. degrees in Electrical Engineering from Politecnico di Torino, Torino, Italy, in 2016 and 2019, respectively. She is currently working toward the Ph.D. degree in Electrical Engineering at the Department of Energy of the Politecnico di Torino. Her main research interests include modelling and control of three-phase and multiphase electrical machines.



Martin Jones received his BEng degree in Electrical and Electronic Engineering (First Class Honors) from the Liverpool John Moores University, UK in 2001. He has been a research student at the Liverpool John Moores University from September 2001 till Spring 2005, when he received his PhD degree. Mr Jones was a recipient of the IEE Robinson Research Scholarship for his PhD studies and is currently

with Liverpool John Moores University as a Reader.



Emil Levi (S'89, M'92, SM'99, F'09) received his MSc and the PhD degrees in Electrical Engineering from the University of Belgrade, Yugoslavia in 1986 and 1990, respectively. He joined Liverpool John Moores University, UK in May 1992 and is since September 2000 Professor of Electric Machines and Drives. He served as a Co-Editor-in-Chief of the IEEE Trans. on Industrial Electronics in the 2009-2013 period.

Currently he is Editor-in-Chief of the IEEE Trans. on Industrial Electronics, Editor-in-Chief of the IET Electric Power Applications and an Editor of the IEEE Trans. on Energy Conversion. He is the recipient of the Cyril Veinott award of the IEEE Power and Energy Society for 2009 and the Best Paper award of the IEEE Trans. on Industrial Electronics for 2008. In 2014 he received the "Outstanding Achievement Award" from the European Power Electronics (EPE) Association and in 2018 the "Professor Istvan Nagy Award" from the Power Electronics and Motion Control (PEMC) Council.